Scientific Research Publishing

Journal of Geoscience and Environment Protection, 2024, 12, 305-321
https://www.scirp.org/journal/gep
ISSN Online: 2327-4344
ISSN Print: 2327-4336

Investigation of the Petrological and Geochemical Characteristics of Siderite in the Early Cretaceous Sandstone of Lacustrine Sedimentary Sequence in the Erlian Basin from Northeastern China

Yunlong Zhang*, Mingming Tian, Huili Xie, Xide Li, Wusheng Liu, Shiqi Ni

Beijing Research Institute of Uranium Geology, Beijing, China
Email: *yunlongzhangbriug@126.com

How to cite this paper: Zhang, Y. L., Tian, M. M., Xie, H. L., Li, X. D., Liu, W. S., & Ni, S. Q. (2024). Investigation of the Petrological and Geochemical Characteristics of Siderite in the Early Cretaceous Sandstone of Lacustrine Sedimentary Sequence in the Erlian Basin from Northeastern China. *Journal of Geoscience and Environment Protection, 12,* 305-321.
https://doi.org/10.4236/gep.2024.126019

Received: May 24, 2024
Accepted: June 25, 2024
Published: June 28, 2024

Abstract

Siderite is a prevalent authigenic mineral in siliciclastic rocks, which usually occurred in eodiagensis period and could be used as an indicator of sedimentary environment. Some siderite precipitated in burial depth with geochemical information of basin fluid evolution. The crystal morphology, geochemical composition, and isotope values are influenced by physical and geochemical environment of precipitation. In this study, samples from the Early Cretaceous of Erlian basin in the northwestern China were collected, and mineralogy, bulk and *in-situ* geochemistry, C and O isotopes were analyzed to comprehensively investigate the sedimentary and diagenetic environment that the sediments experienced. Six lithofaices with three types of crystal habits were recognized in the siderite-rich sandstone, bundle crystal in spherical forms, blocky rhombs in intergranular pore and cleavage of muscovite, and micro bundle and mosaic crystals aggregates in nodular. The siderite growth proceeds through micro bundle and mosaic crystals to bundle siderite aggregates and then into blocky rhombs. The crystal evolution is also reflected by geochemical composition. The micro bundle and mosaic crystals are Ca-siderite. The spheritic shaped bundle aggregates are Ca-Mn-siderite. The blocky rhomb siderite shows gray part and bight part with Ca, Mg and Mn varies. Increase of Ca in block rhomb siderite suggests burial and mesodiagenesis, the high content of Mn may have linkage with eogenetic effects. The relatively positive and slightly negative $\delta^{13}C$ value indicates meteoric water domination and influence of organic matter evolution in shallow buried time. The narrow ranges negative $\delta^{18}O$ value suggest a small span of temperature of siderite formation.

Keywords

Siderite, Sedimentary Environment, Lacustrine Deposition, Early Cretaceous, Erlian Basin

1. Introduction

The widespread occurrence of siderite at the Earth's surface has motivated investigations into the geological and geochemical characteristics, formation, and implication of the siderite in forms of iron formation and cementation (e.g. Jiang et al., 2022; Jiang and Tosca, 2020; Sengupta et al., 2020; Vuillemin et al., 2019; Yang et al., 2021). Siderite grows under a variety of conditions and processes at all stages of burial diagenesis of siliclastic sedimentary sequences (Pe-Piper and Piper, 2020).

Petrologically, authigenic siderite varies in different crystal morphology and aggregation forms, such as rhombohedral and spheroidal (ellipsoid-shaped) siderite, sphaerosiderite, spherulitic siderite and siderite nodules/spheres (e.g. Lim et al., 2004; Mozley and Carothers, 1992; Rodrigues et al., 2015; Shang et al., 2023). The variation has motivated thermodynamic studies for most of the last century. The common conclusion includes that homogeneous Fe(II)-carbonate precipitation is commonly initiated by the nucleation of amorphous iron carbonate at high supersaturation, which appears to provide a favorable surface promoting the secondary growth of more stable crystalline phases. Siderite occurred in these processes depending on solution chemistry (e.g. Dideriksen et al., 2015; Jiang and Tosca, 2019; Jiang and Tosca, 2020).

Siderite usually occurred from eodiagenesis to mesodiagensis, and could developed in marine sediment and nonmarine sediments, which induced variation of chemical composition of the siderite particularly in the content of Mn, Ca, and Mg (e.g. Pe-Piper and Piper, 2020; Stel, 2009; Weibel et al., 2016). The variations in minor elements Mg, Ca and Mn in siderite can be used to track changes in composition of connate water and subsequent basin fluids, and thus could be an indicator of sedimentary and diagenetic environment and basin fluids. Fe-rich siderite usually occurred in marine firmgrounds and pre-compaction concretion of mudstones. Mg-rich siderite cement suggests the sediment experienced diagenesis and the basin fluid evolved. Ca-rich siderite is more common, demonstrating a link to formation waters (Pe-Piper and Piper, 2020). Magnesium-rich siderite is reported to form at higher temperatures than Ca-rich or Fe-rich varieties (Morad, 1998).

The variation of sedimentary environment and pore fluid evolution influence the diffraction of C and O isotope. The statistic shows that $\delta^{13}C$ and $\delta^{18}O$ value of siderite from marine and nonmarine sediments overlap but also could be significantly recognized. The siderite from marine environment has more negative $\delta^{13}C$ that in nonmarine siderite, whilst the value of $\delta^{18}O$ is commonly negative in

nonmarine siderite (Mozley and Carothers, 1992; Mozley and Wersin, 1992). The strongly negative $\delta^{13}C$ value of siderite suggests carbon from microbial degradation of organic matter in the sub-oxic and sulphate reduction conditions (Mozley and Carothers, 1992; Pe-Piper and Piper, 2020).

Combining all these investigations of the siderite, including lithological facies, crystal morphology, geochemical characteristics and isotope composition, a reasonable comprehensive method was established to interpret the sedimentary and diagenesis environment that the sediments undergone. Thus, in this study, a sequence of lacustrine sediments including sandstone and mudstone was selected from the Early Cretaceous in the Erlian basin to conduct the analysis focusing on siderite occurred in aiming at further understanding of the environment and basin evolution. The sedimentary background constraints the lacustrine sedimentary environment, which narrowed the interpretation and induced more reliable conclusions.

2. Geological Setting

The Erlian Basin is located in northeastern China (**Figure 1**), Inner Mongolia, near the border of China and Mongolia. The Erlian Basin is a Mesozoic-Cenozoic intracontinental faulted basin, developed on Hercynian folded basement corresponding to the southern margin of the Xing Mongolian orogenic belt during the Mesozoic continental extension of eastern Asia, which is located on the suture between the Asian and Siberian plates (Wang et al., 2019). It comprises more than 40 north-northeast trending subbasins ranging from 150 to 4200 km^2 in basin area (Ding et al., 2015). It comprises five major sub-basins: the Chuanjing Sub-basin to the west, the Wulanchabu Sub-basin in the central-west, the Manite Sub-basin in the central-north, the Tengge'er Sub-basin in the south-east and the Wunite Sub-basin to the north-east (Bonnetti et al., 2014).

The basin mainly developed in three stages controlled by normal-fault system: (i) a pre-rift stage mainly characterized by the emission of Late Jurassic to very Early Cretaceous volcanic rocks of the Qinganling Group (156.0 - 142.6 Ma); (ii) a syn-rift stage characterized by the deposition of Early Cretaceous sedimentary units; and (iii) a post-rift stage characterized by a switch from tectonic to thermal subsidence and the deposition of the Cretaceous sequence.

The Lower Cretaceous is composed of the Aershan, Tengger, and Saihantala Formations (**Figure 1**), consisting of conglomerates, sandy conglomerates, sandstones, siltstones, mudstones, shales, and coals, with a total thickness of 2100 - 4500 m. The ages of Aershan, Tengger, and Saihantala Formations (124 - 105.5 Ma) correspond to the lower and upper part of the Aptian and most of the Albian, respectively (Wang et al., 2019). The overlying Erlian Formation developed in the Early Cretaceous includes a lower member dominated by sandstone and an upper member dominated by mudstone (Bonnetti et al., 2015). After the deposition of the Early Cretaceous sequence, the uplift stopped lacustrine deposition and the basin evolved into the stage of erosion and weathering.

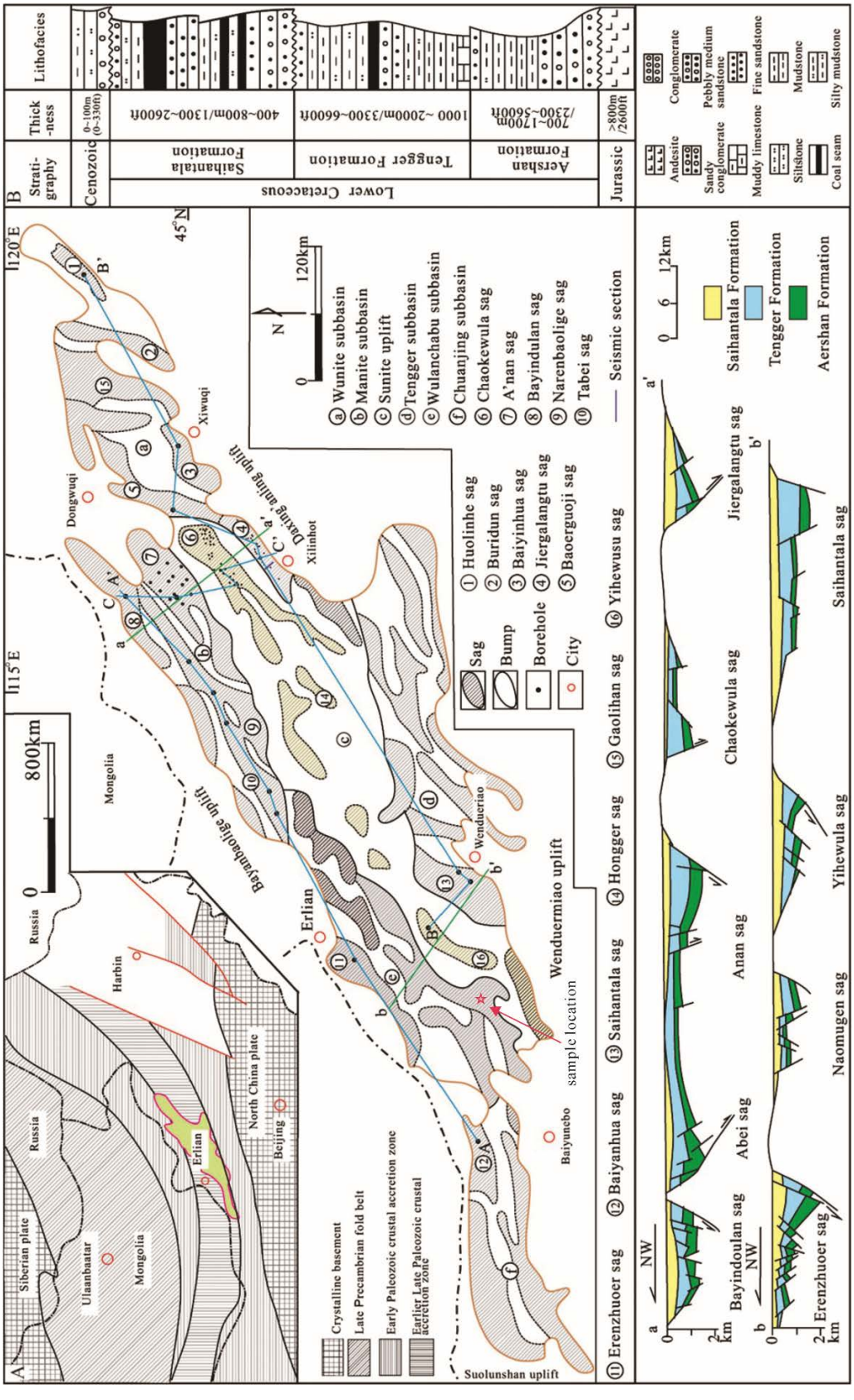

Figure 1. Geological setting, tectonics and sedimentary sequence of Erlian basin. (A) Tectonic setting and sub-depression of the basin; (B) Sedimentary formation and lithology (after Wang et al., 2019).

3. Samples and Methods

3.1. Samples

There are 66 samples were collected from core sequence of a drilled well in the Wulanchabu sub-basin. Samples were collected onsite and reserved in sealed bags with name tags including information of lithology, location and specific depth. The sedimentary information of the sampled cores was logged, and the lithological sequence is in **Figure 2**.

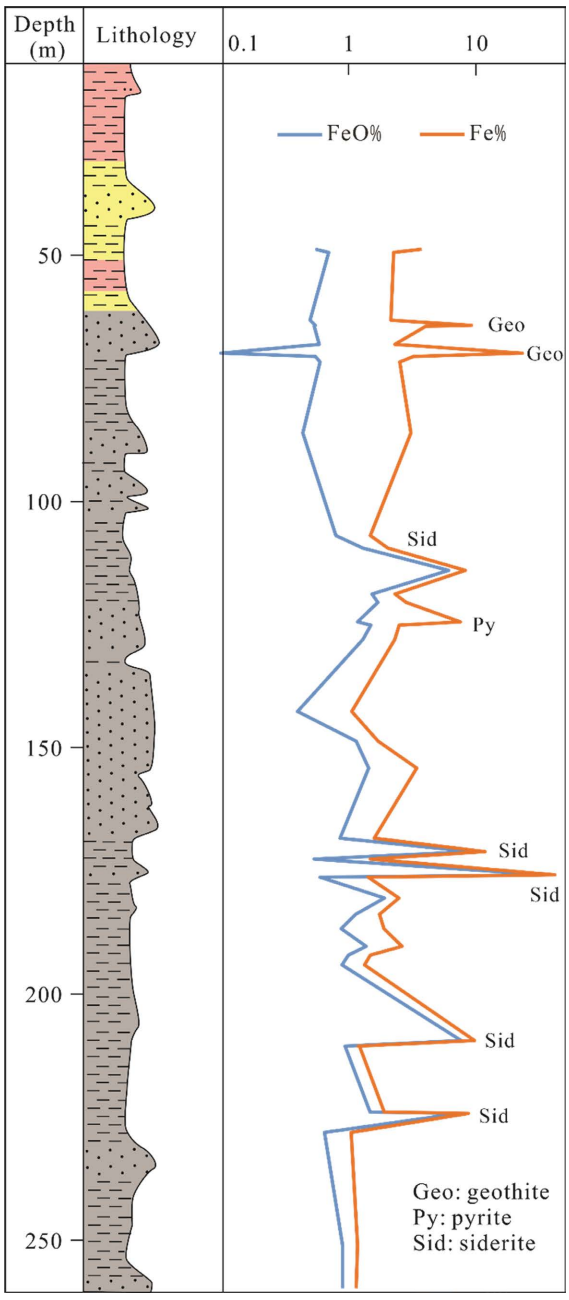

Figure 2. The sedimentary sequence and lithology column from drilling core where samples were collected, which subject to Sahantala formation, the curve of content of total Fe and FeO were derived from geochemical analysis results.

3.2. Methods

3.2.1. Petrographic and Mineralogical Analysis

Optical petrographic microscope Leica DM4 P and scanning electron microscope (SEM) Zeiss Sigma 300 equipped with a Bruker XFlash 6130 probe for energy dispersive X-ray spectrometry analysis were used for the petrology and mineralogy analysis. The SEM samples were coated with carbon using a Leica EM ACE500 for preparation. SEM analysis was performed at an energy of 20 kV and a probe work distance of 8 - 10 mm.

3.2.2. Bulk and *In-Situ* Geochemical Analysis

The major element content of the bulk sedimentary rock samples was analyzed using X-ray fluorescence (XRF). A portion of the crushed and dried sample (0.7 g) was blended with anhydrous lithium tetraborate (5.2 g), lithium fluoride (0.4 g), and ammonium nitrate (0.3 g) that had been dried at 105˚C for 2 to 4 h. The blended mixture was then mixed with 1 mL of lithium bromide solution, dried, and finally fused in Pt/Au crucibles for 10 to 15 min until completely melted. The resulting melted sample was transferred to a pre-heated Pt/Au mold and cooled with compressed air. The samples were analyzed by using an AB104 Axios-MAX X-ray fluorescence spectrometer (PANalytical, Almelo, Netherlands) at a voltage of 50 kV and a current of 50 mA. The loss of ignition (LOI) was calculated based on the theoretical coefficient of loss of ignition (α). The detection limit for all major components was estimated to be approximately part per million level.

The trace and minor element content of the bulk samples were analyzed utilizing Inductively Coupled Plasma Mass Spectrometry (ICP-MS) on a NexIon300D instrument (Perkin-Ilmer, Waltham, MA, USA). The process involved preparing a 0.100 g powder sample, which was added to a lithium metaborate/lithium tetraborate flux and fused in a furnace at 1025˚C. The resulting melt was then cooled and dissolved in an acid mixture composed of nitric, hydrochloric, and hydrofluoric acids, and subjected to analysis. The Loss of Ignition (LOI) was determined by weighing the samples before and after ignition at 1000˚C. The analytical precision was found to vary around 0.001 ppm.

In-situ element analysis was conducted on the siderite selected in the thin sections, which was ablated by a 32 μm laser beam with a mixed H_2/He as a carrier gas. The resulting aerosol, composed of the carrier gas and ablated sample, was introduced into the inductively coupled plasma mass spectrometry (ICP-MS) for elemental signal collection. Each cycle of the signal collection included a 10-second blank and a 20-second sample signal. Elemental abundances were calibrated using National Institute of Standards and Technology (NIST) standard reference materials, SRM 610, SRM 612, and NIST 610. Internal corrections were applied to correct for matrix effects, using the Ca content determined by electron probe micro-analysis (EPMA). The data was processed using ICPMSDataCal and multiple external standards-signal internal standard methods. The detection limit for this analysis is at the parts-per-billion (ppb) level (Zhang et al.,

2023).

3.2.3. Isotope Analysis

The C and O isotopes were analyzed according to the methods for carbonate C and O isotope analyses. The powdered sample was digested with H_3PO_4 and was analyzed using a Kiel IV device attached to a Thermo MAT 253 mass spectrometer that is equipped with a dual inlet system. The liberated CO_2 was carried by He. All conventional stable isotope values are expressed using the standard per mil notation and are reported here based on the Vienna Peedee Belemnite (VPDB) standard. The accuracy of the measurement is ±0.1% for the $\delta^{13}C$ and ±0.2% for the $\delta^{18}O$.

4. Results and Discussion

4.1. Petrology and Mineralogy of the Bulk Rock

Generally, sandstone and mudstone composed the sedimentary sequence of the lacustrine rocks in research area. XRD analysis indicated that quartz, plagioclase, and clay minerals are the main mineral component. In the sandstone samples (n = 42), the content of quartz is ranging from 10% to 71% with an average of 50%, the content of plagioclase is ranging from 3% to 40% with an average of 16%, and the content of clay minerals is ranging from 11% to 58% with an average of 30%. The high content of plagioclase demonstrated low component maturity of these rocks. Relatively high content of clay minerals implies low component maturity or the intensive fluid-rock reaction and relatively high degree of diagenesis of the samples.

In the clay minerals, illite and illite/smectite are the majorities, which ranges between 14% and 89% with an average of 54%, and between 7% and 50% with an average of 30% respectively. Then kaolite content ranks in third with an average of 15%. These results demonstrate that the total clay mineral content is relatively high in the bulk sandstone, and within the clay minerals, illite and illite/smectite are predominant.

The investigation of the formation of illite in sandstone shows that reaction between K-feldspar and kaolinite at elevated temperatures are the main mechanism of illite formation (Inoue et al., 1988; Pollastro, 1985). The control factors of the alteration include openness and closeness of the system, the temperature, and the source of potassium etc. In a closed system, temperature is the main control factor. The transition from incipient to extensive illitization in these sandstones is associated with a present burial depth of 3.7 km, corresponding to a formation temperature of 140˚C (Ehrenberg, 1989). In an open system, the additional supply of K^+ is a key factor promoting the precipitation of illite (Ehrenberg, 1989). These imply that the samples in research area are likely experienced deep burial and diagenesis in depth, or they may be abrupted by extra potassium fluid after deposition.

The petrological analysis shows abundant clay component and matrix filled intergranular pores (**Figure 3(a)**), however there's no significant morphology of

illite or smectite, which could be observed. The mica is slightly occurred in bending however lacking of alteration, which also reflected by less chlorite was detected by using an XRD. The significant cement minerals are siderite, goethite and pyrite (**Figures 3(b)-(d)**), they are sporadically enriched in the intervals in the sedimentary column (**Figure 2**). The less compacted structure and lack of cementation development indicate that the samples in research area undergone a weak diagenesis process. Comparing with the characteristic of high content of illite and illite/smectite, which plausibly implies a certain degree of diagenesis in particular geochemical and geophysical condition, petrological analysis indicated less diagenesis influence, which suggests that the illite and illite/smectite may come from the detrital sedimentary component rather than authigenic.

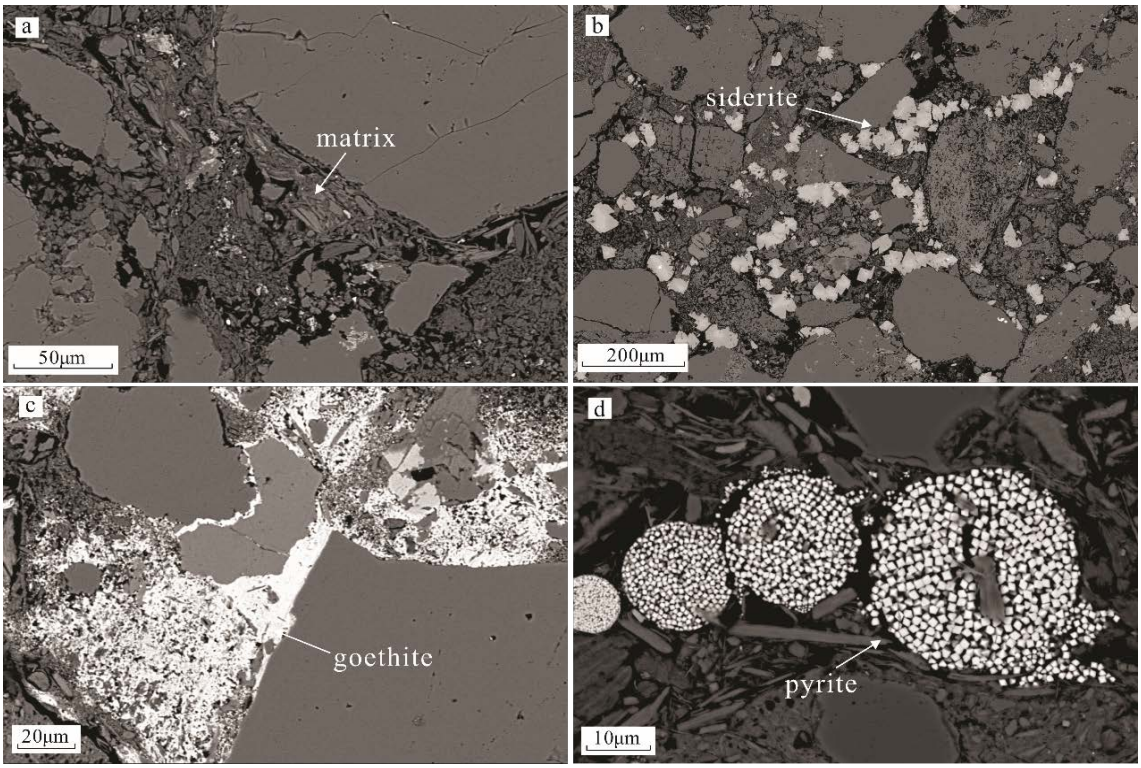

Figure 3. Microphotographs of sandstone in research area. (a) sandstone with matrix filling the intergranular pores; (b) Authigenic siderite cement; (c) Authigenic goethite cements; (d) Authigenic framboid pyrite cement.

4.2. Siderite Occurrence and Facies

4.2.1. Facies of Siderite-Bearing Rocks

There are six facies of siderite were recognized in the sandstone samples based on the morphology and texture of the crystalline in study area, including facies 1: high content of spheritic shaped siderite aggregation with radial texture (**Figure 4(a)**), facies 2: angular siderite aggregation with radial texture (**Figure 4(b)**), facies 3: spheritic shaped siderite aggregation with pyrite as core (**Figure 4(c)**), facies 4: euhedral crystalline siderite (**Figure 4(d)**), facies 5: sim-euhedral, euhedral crystalline siderite filling in biotite (**Figure 4(e)**), facies 6: siderite nodular aggregation (**Figure 4(f)**), These facies are separately occurred in different samples

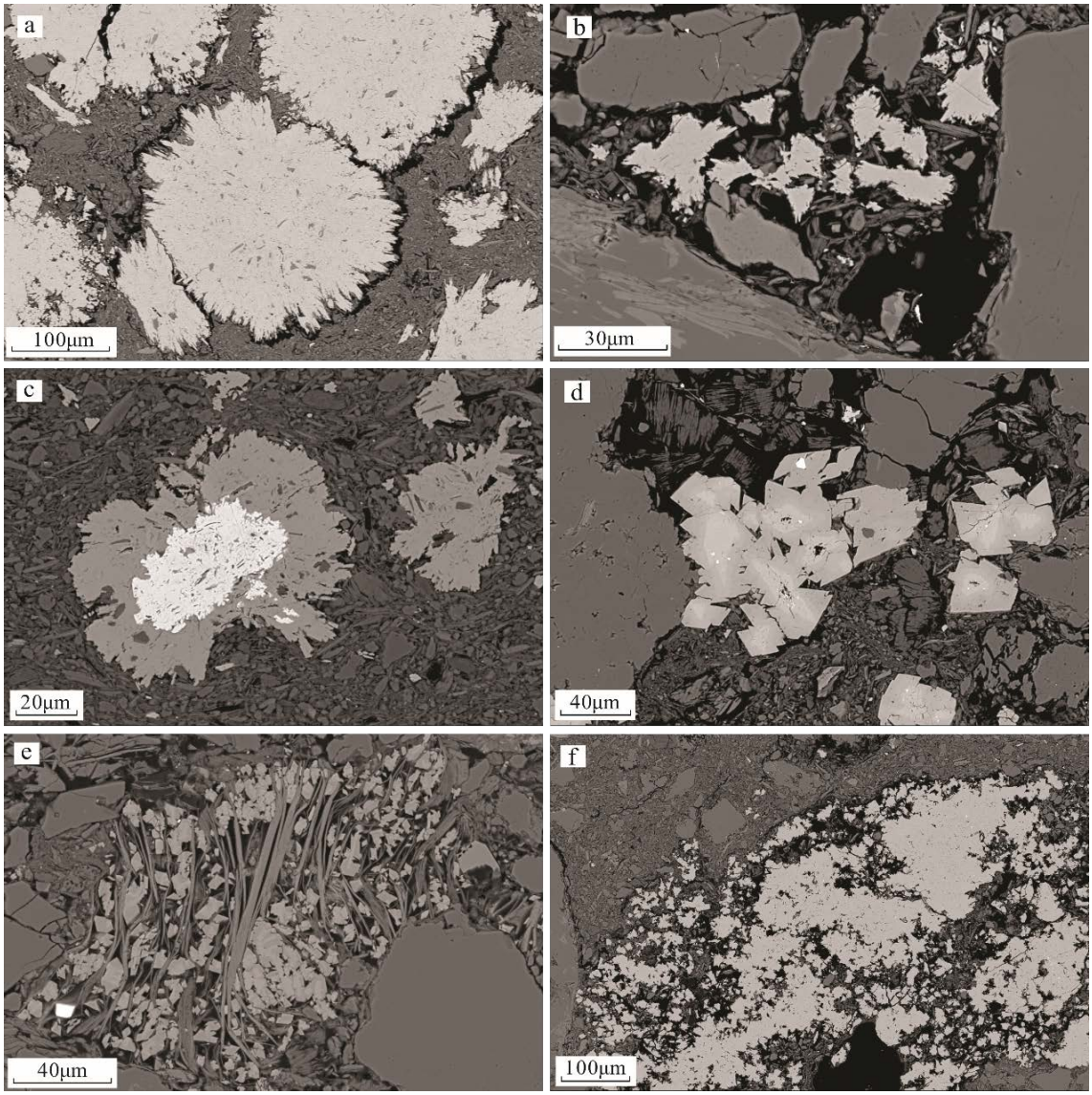

Figure 4. Microphotographs of siderite facies. (a) Spheritic shaped siderite aggregation with radial texture; (b) Angular siderite aggregation with radial texture; (c) Spheritic shaped siderite aggregation with pyrite as core; (d) Euhedral crystalline siderite in intergranular pores; (e) Sim-euhedral, euhedral crystalline siderite filling in biotite; (f) Siderite nodular aggregation.

that with high content of siderite.

4.2.2. Variation in Crystal Habits of Siderite

In these facies, the crystal habits of siderite are mainly three types. Bundle crystal, which usually aggregated in spherical forms and occurred in intergranular pores of fine sandstone and abundantly gathered in mudstone (e.g. Facies, 1, 2 and 3, **Figures 4(a)-(c)**). Blocky rhombs, which was observed in the intergranular pores and in the cleavage of muscovite, usually occurred in twin or in crystal stock with chemical zonation and oriented in the muscovite cleavage (e.g. Facies, 4 and 5, **Figure 4(d)** and **Figure 4(e)**). Micro bundle and mosaic crystals, which fund as spheroidal aggregates, usually developed as facies 6 (**Figure 4(f)**) in fine

sediments.

Diagenetic maturation results in an increasing crystallinity of siderites (Vuillemin et al., 2019). During the diagenesis, siderite growth proceeds through microspar-sized precursor crystals into larger spar mosaic-type crystals, and further into bundles and spheroidal clusters (Vuillemin et al., 2019). The morphology of siderite crystals in the research area shows that micro bundle and mosaic crystals have the lowest maturation, the bundle siderite aggregates have moderate maturation and the blocky rhombs occurred in twin or in crystal stock have the highest maturation.

4.2.3. Formation of Siderite

Siderite is common carbonate precipitation in reduced environment with high Fe^{2+} and bicarbonate concentrations (Mulders et al., 2021). The experiment shows that the precipitation of siderite is from dehydration and crystallization of the amorphous ferrous carbonates, which initially precipitates in the supersaturation condition (Montes-Hernandez and Renard, 2016). The morphology and crystallinity of the precipitated phases are affected by the nucleation mechanism and time (Guo et al., 2010). At indoor temperature, siderite is nearly 7-orders of magnitude slower than that of calcite (Jiang and Tosca, 2020). The precipitation rate of siderite varies balancing the concentration of Fe(II) in pore fluid, and thus the concentration of Fe(II) in pore fluid could be responded by the content of siderite. The extremely high content of siderite in episodic core intervals indicates the reduced environment and extra Fe supply event occurred, which could be dissimilatory iron reduction, hydrothermal activity, or dissolution of other Fe(II) minerals.

4.3. *In-Situ* Element Analysis

The five samples with different type of siderites were analyzed by EPMA. In the spheritic shaped siderite aggregation, cross-grain *in-situ* analysis shows that Fe content increases from the core outside with a range of 51.6 wt% - 57.4 wt%. The content of Mn significantly decreases with a range of 0.3 wt% - 5.5 wt%. Ca content slightly varies but has significant decrease on the rim, which ranges from 2.7 wt% to 6.1 wt% (**Figure 5**). The content of Mg remains constant across the spheritic siderite aggregation with a low content of ranging from 0.1 wt% to 0.2 wt% (n = 19).

In the siderite bundles aggregated in angular grain forms and in spherical forms with pyrite as a core, and in the micro bundle and mosaic crystals siderite aggregated in nodular, the content of Ca and Fe has a less variation from spot to spot. The content of CaO ranges from 2.57 wt% to 6.34 wt% with an average of 3.88 wt%; and the FeO content ranges from 46.76 wt% to 56.73 wt% with an average of 54.81 wt% (n = 30). The content of Mn is extremely heterogeneous distributed on the grains. On the most analyzed spots (26 out of 30), the MnO content is located in the range of 0.xx wt%, and most of them are less than 0.5 wt%, however, sporadic spots (4 out of 30) demonstrate very high content of with one

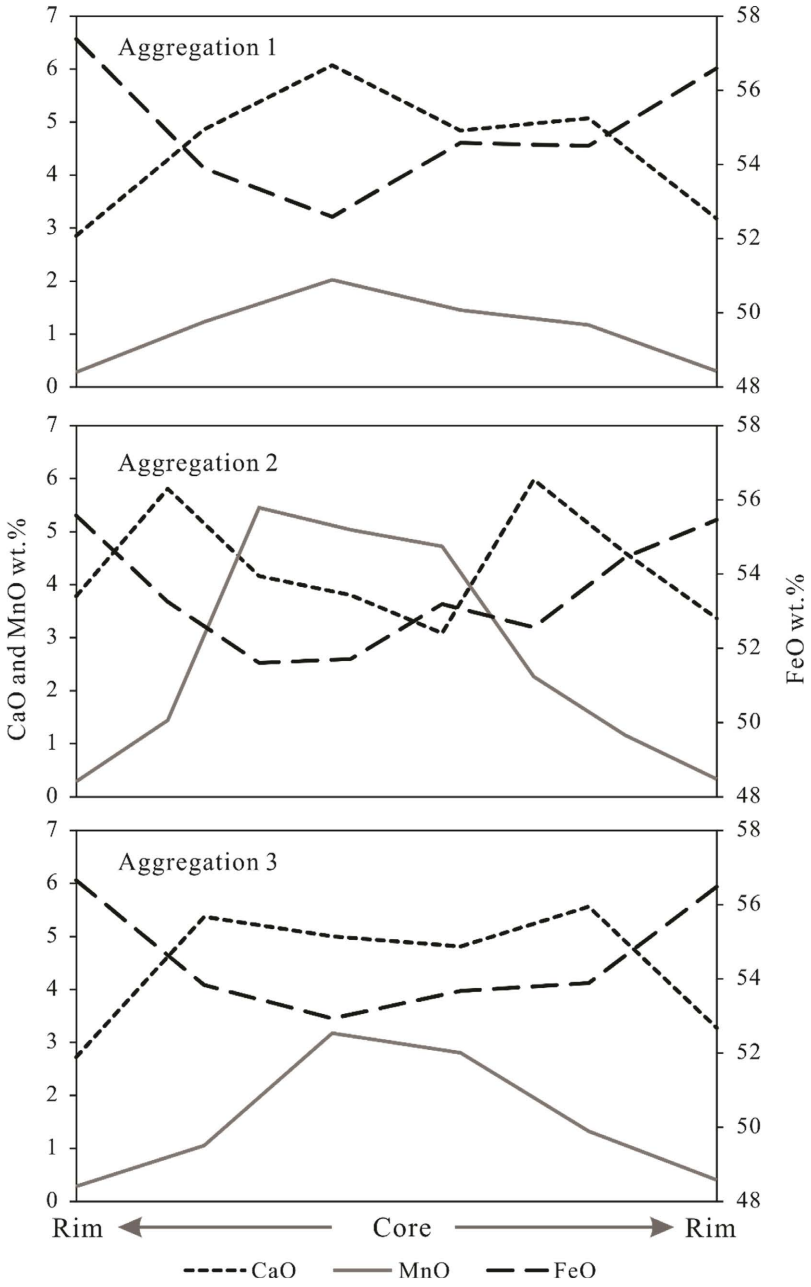

Figure 5. *In-situ* element analysis results from three spheritic shaped siderite aggregation with bundle crystals. The *in-situ* analysis sites crossed the siderite grains and obtained the element distribution with the growth of the grains.

order of magnitude higher than the other spots.

The blocky rhomb siderite in the cleavage of muscovite could be significantly recognized with two different parts under the SEM, the bright part and gray part. The difference is on account of the geochemical composition. The bright part has low content of Mg that is about 0.1 to 0.2 wt% (n = 9), similar with that in the bundle siderite aggregation in facies 1, 2 and 3. The gray part has relatively high content of Mg that is about 7 to 10.7 wt% with an average of 8 wt% (n = 9). The bright part has relatively low content of Ca that is about 1.3 wt% to 3.7 wt%

with an average of 2.6 wt% (n = 9), which is slightly higher in gray part with a range of 3.2 - 5.5 wt% and 4.8 wt% on average (n = 9). The increase of Mg and Ca content in the gray part induced significant decrease of Fe content, which is demonstrated with a range of 44 - 46 wt%, nearly 10 percent less than in the bright part ranging from 52 to 57 wt%. The content of Mn is varying in the both parts, but is slightly higher in the bright part with an average of 2.2 wt%, comparing to the gray part of 1.1 wt% on average.

The blocky rhomb siderite in the pores also could be recognized in gray and bright parts significantly. The bright part usually composes the core the the rhomb, and the gray part is in the outer zone. The gray part has relatively higher content of Ca and Mg than the bright part. The Ca content is from 4.3 wt% to 8 wt% and 6.4 wt% on average (n = 10) in gray part and is from 2.1 wt% to 3.9 wt% and 2.8 wt% on average (n = 10) in bright part, nearly half of that in gray part. The Mg content is from 5.3 wt% to 8.1 wt% and 6.6 wt% on average (n = 10) in gray part however is less than 0.2 wt% in bright part. The content of Mn in both parts are less than 0.4 wt%, which is significantly different from that of the blocky rhomb siderite in the muscovite cleavage.

Comparing to the element content and characterizing the siderite with the relatively high element of Ca, Mg, Mn, the siderite has bundles aggregated in angular grain forms and in spherical forms with pyrite as a core, and siderite nodular with micro bundle and mosaic crystals are Ca-siderite due to the relatively high content of Ca. Similarly, the spheritic shaped bundle aggregates are Ca-Mn-siderite; the gray part of the blocky-rhomb siderite in muscovite cleavage is Ca-Mg-Mn-siderite; and the bright part is Mn-siderite. The gray part of the blocky-rhomb siderite in pores is Ca-Mg-siderite, and the bright part is the ordinary siderite with Ca, Mg and Mn content relatively the lowest.

The variation of chemical composition of siderite is primarily on account of the Fe^{2+}, Mg^{2+}, Mn^{2+}, and Ca^{2+} ions concentration in the pore waters (Mozley, 1989). Meteoric water is characterized by high amounts of Ca, but little Mg, which is consistent with the concentration of Ca and Mg in the bundle siderite aggregates in facies 1, 2, 3 and 6. Additionally, the lack of compaction allows siderite precipitates rapidly and forming aggregates in larger size near after deposition, which implied that the facies 1, 2, 3 and 6 are occurred in the eogenetic stage. Experiments showed that Mg uptake was not observed at 20˚C, but increased slightly at 55˚C (Sengupta et al., 2020). The content of Mg significantly increased in the gray parts Facies 4 and 5 siderite, which indicates that the rhomb siderite precipitated in burial depth with the temperature increased. And the high Mg concentration is possibly from evolved formation water (El-Ghali et al., 2006; Rossi et al., 2001). Breakdown of K-feldspar and conversion of Mg-smectite, and largely of volcanic origin to illite can release Mg ions to formation water (Bowman et al., 2012; Pe-Piper and Piper, 2020). The high concentration of Mn observed in eogenetic siderite (Facies 1) and bright part of buried siderite in muscovite cleavage (Facies 5). The occurrence of Mn-rich siderite implies either variation in redox conditions or presence of some residual earlier

siderite (Pe-Piper and Piper, 2020).

4.4. C and O Isotopes

There has negligible content of carbonate minerals that were observed in the siderite samples by XRD. We can suppose that siderite dominates the origin carbon dioxide for the C O isotope analysis, and thus the isotope of the bulk sample could be recognized as the isotope of the siderite within. The $\delta^{13}C$ and $\delta^{18}O$ results are expressed in relative to the standard Vienna Pee Dee Belemnite (VPDB). Five samples of siderite ranges from −1‰ to 11.8‰ in $\delta^{13}C$ and −12.8‰ to −10‰ in $\delta^{18}O$. The other sandstone samples range from −10.8‰ to 13.8‰ in $\delta^{13}C$ and −18.1‰ to −9.2‰ in $\delta^{18}O$ (n = 26) (**Figure 6**).

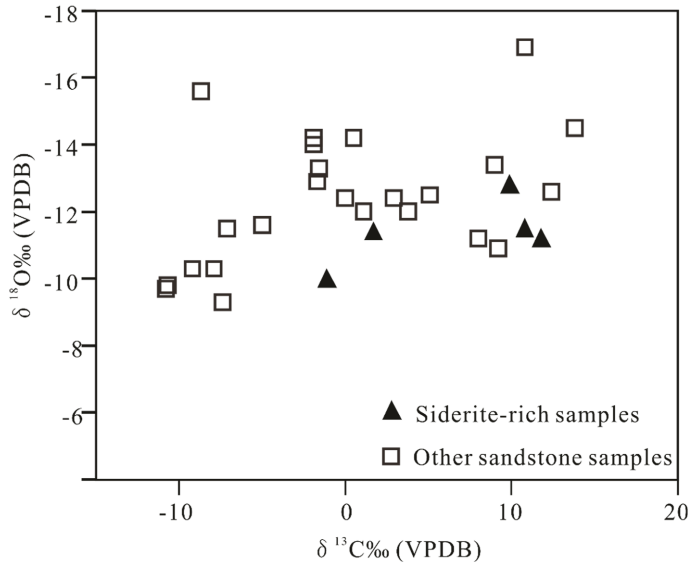

Figure 6. The cross plot of C and O isotope values from all sandstone samples with five siderite rich samples marked.

The C and O isotope of siderite is an indicator of sedimentary environment. Siderites with $\delta^{13}C$ values < −8‰ are suggested most likely of marine origin, whereas those with $\delta^{18}O$ values < −13‰ with positive $\delta^{13}C$ values are most likely of nonmarine origin (Mozley and Wersin, 1992). The values of $\delta^{13}C$ and $\delta^{18}O$ in research area are consistent with statistic result of nonmarine sedimentary environment values. The sequenced sampling from the drilling core shows an increase of $\delta^{13}C$ value from top to depth. The lower $\delta^{13}C$ value on the top part suggest the influence of meteoric water (−7‰ - −3.5‰) (Schmidt et al., 2005) or decarboxylation of organic matter (−10‰ - −25‰) (Irwin et al., 1977). The increasing and positive $\delta^{13}C$ value in the depth suggest the dissolved carbon from lacustrine water (2.9‰ - 9.3‰) (Lyu et al., 2018; Tian et al., 2018) or microbial fermentation of organic matter (8‰ - 23‰) (Macaulay et al., 2018) may performed as C sources for the cement (Xi et al., 2019). This indicates that relatively positive and slightly negative $\delta^{13}C$ value in the siderites were influenced by sedimentary pore water, meteoric water and organic matter evolution in shallow

buried time.

Oxygen isotope can act as a geological thermometer measuring the formation temperature of authigenic minerals in sandstone reservoirs (Xi et al., 2019). The span of the $\delta^{18}O$ value is narrower than that of the $\delta^{13}C$ value in siderite samples and others. Assumed that the micro calcite dominated carbon and oxygen isotope value came out from the method using phosphorus acid as dissolving agent, the model for calcite-H_2O reaction proposed by Friedman and O'Neil (1977) to do the paleotemperature calculation suggest a narrow thermal range of siderite precipitation in research area.

5. Conclusion

The samples contain relatively high content of clay minerals with detrital illite and illite/smectite domination indicating low composition maturity, which is consistent with the generally characteristics of lacustrine sediments in rift basin. Siderite bearing samples could be recognized in 6 facies, which also a classification of siderite occurrence, including crystal morphology, aggregation, and content. Mainly three types of crystal habits of siderite were recognized including bundle crystal, which usually aggregated in spherical forms, blocky rhombs in intergranular pores and cleavage of muscovite, and micro bundle and mosaic crystals aggregates in nodular. The habits of the crystal suggest the siderite growth proceeds through micro bundle and mosaic crystals to bundle siderite aggregates and then into blocky rhombs. The blocky rhombs suggest burial diagenesis occurred.

Geochemically, the micro bundle and mosaic crystals in nodular form are Ca-siderite due to the relatively high content of Ca. The spheritic shaped bundle aggregates are Ca-Mn-siderite. The blocky rhomb siderite shows gray part and bight part in SEM. The crystals in muscovite cleavage are Ca-Mg-Mn-siderite of the gray part and Mn-siderite of the bright part. The crystals in intergranular pores are different, which shows Ca-Mg-siderite in gray part and ordinary Fe-siderite with low content of Ca, Mg and Mn. The primary pore fluid dominated the precipitation o Ca-siderite. Burial and mesodiagenesis increased the content of Mg with the increase of crystallization. The high content of Mn in siderite may have linkage with eogenetic effects.

The relatively positive and slightly negative $\delta^{13}C$ value in the siderites were influenced by sedimentary pore water, meteoric water and organic matter evolution in shallow buried time. The narrow ranges negative $\delta^{13}O$ value suggest a small span of temperature of siderite formation.

Conflicts of Interest

The authors declare no conflicts of interest regarding the publication of this paper.

References

Bonnetti, C., Cuney, M., Malartre, F., Michels, R., Liu, X., & Peng, Y. (2015). The Nuhet-

ing Deposit, Erlian Basin, NE China: Synsedimentary to Diagenetic Uranium Mineralization. *Ore Geology Reviews, 69,* 118-139. https://doi.org/10.1016/j.oregeorev.2015.02.010

Bonnetti, C., Malartre, F., Huault, V., Cuney, M., Bourlange, S., Liu, X. et al. (2014). Sedimentology, Stratigraphy and Palynological Occurrences of the Late Cretaceous Erlian Formation, Erlian Basin, Inner Mongolia, People's Republic of China. *Cretaceous Research, 48,* 177-192. https://doi.org/10.1016/j.cretres.2013.09.013

Bowman, S. J., Pe-Piper, G., Piper, D. J. W., Fensome, R. A., & King, E. L. (2012). Early Cretaceous Volcanism in the Scotian Basin. *Canadian Journal of Earth Sciences, 49,* 1523-1539. https://doi.org/10.1139/e2012-063

Dideriksen, K., Frandsen, C., Bovet, N., Wallace, A. F., Sel, O., Arbour, T. et al. (2015). Formation and Transformation of a Short Range Ordered Iron Carbonate Precursor. *Geochimica et Cosmochimica Acta, 164,* 94-109. https://doi.org/10.1016/j.gca.2015.05.005

Ding, X., Liu, G., Zha, M., Huang, Z., Gao, C., Wang, P. et al. (2015). Characteristics and Origin of Lacustrine Source Rocks in the Lower Cretaceous, Erlian Basin, Northern China. *Marine and Petroleum Geology, 66,* 939-955. https://doi.org/10.1016/j.marpetgeo.2015.08.002

Ehrenberg, S. N. (1989). Formation of Diagenetic Illite in Sandstones of the Garn Formation, Haltenbanken Area, Mid-Norwegian Continental Shelf. *Clay Minerals, 24,* 233-253.

El-Ghali, M. A. K., Tajori, K. G., Mansurbeg, H., Ogle, N., & Kalin, R. M. (2006). Origin and Timing of Siderite Cementation in Upper Ordovician Glaciogenic Sandstones from the Murzuq Basin, SW Libya. *Marine and Petroleum Geology, 23,* 459-471. https://doi.org/10.1016/j.marpetgeo.2006.02.002

Friedman, I., & O'Neil, J. (1977). *Compilation of Stable Isotope Fractionation Factors of Geochemical Interest*.

Guo, H., Li, Y., & Zhao, K. (2010). Arsenate Removal from Aqueous Solution Using Synthetic Siderite. *Journal of Hazardous Materials, 176,* 174-180. https://doi.org/10.1016/j.jhazmat.2009.11.009

Inoue, A., Velde, B., Meunier, A., & Touchard, G. (1988). Mechanism of Illite Formation during Smectite-to-Illite Conversion in a Hydrothermal System. *American Mineralogist, 73,* 1325-1334.

Irwin, H., Curtis, C., & Coleman, M. (1977). Isotopic Evidence for Source of Diagenetic Carbonates Formed during Burial of Organic-Rich Sediments. *Nature, 269,* 209-213. https://doi.org/10.1038/269209a0

Jiang, C. Z., & Tosca, N. J. (2019). Fe(II)-Carbonate Precipitation Kinetics and the Chemistry of Anoxic Ferruginous Seawater. *Earth and Planetary Science Letters, 506,* 231-242. https://doi.org/10.1016/j.epsl.2018.11.010

Jiang, C. Z., & Tosca, N. J. (2020). Growth Kinetics of Siderite at 298.15 K and 1 Bar. *Geochimica et Cosmochimica Acta, 274,* 97-117. https://doi.org/10.1016/j.gca.2020.01.047

Jiang, C. Z., Halevy, I., & Tosca, N. J. (2022). Kinetic Isotope Effect in Siderite Growth: Implications for the Origin of Banded Iron Formation Siderite. *Geochimica et Cosmochimica Acta, 322,* 260-273. https://doi.org/10.1016/j.gca.2022.01.029

Lim, D. I., Jung, H. S., Yang, S. Y., & Yoo, H. S. (2004). Sequential Growth of Early Diagenetic Freshwater Siderites in the Holocene Coastal Deposits, Korea. *Sedimentary Geology, 169,* 107-120. https://doi.org/10.1016/j.sedgeo.2004.05.002

Lyu, F., Liu, C., Jiao, P., Zhang, H., Sun, X., & Zhang, Y. (2018). Carbon and Oxygen Iso-

topic Compositions of the Lacustrine Carbonate in Lop Nur since the Mid-Pleistocene and Their Paleoenvironment Significance. *Acta Geologica Sinica, 93,* 1589-1604.

Macaulay, C. I., Fallick, A. E., Haszeldine, R. S., & McAulay, G. E. (2018). Oil Migration Makes the Difference: Regional Distribution of Carbonate Cement $\Delta^{13}C$ in Northern North Sea Tertiary Sandstones. *Clay Minerals, 35,* 69-76. https://doi.org/10.1180/000985500546738

Montes-Hernandez, G., & Renard, F. (2016). Time-Resolved *in Situ* Raman Spectroscopy of the Nucleation and Growth of Siderite, Magnesite, and Calcite and Their Precursors. *Crystal Growth & Design, 16,* 7218-7230. https://doi.org/10.1021/acs.cgd.6b01406

Morad, S. (1998). *Carbonate Cementation in Sandstones: Distribution Patterns and Geo-Chemical Evolution* (pp. 1-26). The International Association of Sedimentologists.

Mozley, P. S. (1989). Relation between Depositional Environment and the Elemental Composition of Early Diagenetic Siderite. *Geology, 17,* 704-706.

Mozley, P. S., & Carothe, W. W. (1992). Elemental and Isotopic Composition of Siderite in the Kuparuk Formation, Alaska: Effect of Microbial Activity and Water/Sediment Interaction on Early Pore-Water Chemistry. *Journal of Sedimentary Petrology 62,* 681-692. https://doi.org/10.1306/d4267988-2b26-11d7-8648000102c1865d

Mozley, P. S., & Wersin, P. (1992). Isotopic Composition of Siderite as an Indicator of Depositional Environment. *Geology, 20,* 817-820. https://doi.org/10.1130/0091-7613(1992)020<0817:icosaa>2.3.co;2

Mulders, J. J. P. A., Tobler, D. J., & Oelkers, E. H. (2021). Siderite Nucleation Pathways as a Function of Aqueous Solution Saturation State at 25 ˚C. *Chemical Geology, 559,* Article ID: 119947. https://doi.org/10.1016/j.chemgeo.2020.119947

Pe-Piper, G., & Piper, D. J. W. (2020). Significance of the Chemistry and Morphology of Diagenetic Siderite in Clastic Rocks of the Mesozoic Scotian Basin. *Sedimentology, 67,* 782-809. https://doi.org/10.1111/sed.12661

Pollastro, R. M. (1985). Mineralogical and Morphological Evidence for the Formation of Illite at the Expense of Illite/Smectite. *Clays and Clay Minerals, 33,* 265-274. https://doi.org/10.1346/ccmn.1985.0330401

Rodrigues, A. G., De Ros, L. F., Neumann, R., & Borghi, L. (2015). Paleoenvironmental Implications of Early Diagenetic Siderites of the Paraíba Do Sul Deltaic Complex, Eastern Brazil. *Sedimentary Geology, 323,* 15-30. https://doi.org/10.1016/j.sedgeo.2015.04.005

Rossi, C., Marfil, R., Ramseyer, K., & Permanyer, A. (2001). Facies-Related Diagenesis and Multiphase Siderite Cementation and Dissolution in the Reservoir Sandstones of the Khatatba Formation, Egypt's Western Desert. *Journal of Sedimentary Research, 71,* 459-472. https://doi.org/10.1306/2dc40955-0e47-11d7-8643000102c1865d

Schmidt, M., Xeflide, S., Botz, R., & Mann, S. (2005). Oxygen Isotope Fractionation during Synthesis of CaMg-Carbonate and Implications for Sedimentary Dolomite Formation. *Geochimica et Cosmochimica Acta, 69,* 4665-4674. https://doi.org/10.1016/j.gca.2005.06.025

Sengupta, R., Tosca, N. J., & Robinson, S. A. (2020). Geochemical Controls on the Elemental Composition of Siderite: Implications for Palaeo-Environmental Reconstructions. *Geochimica et Cosmochimica Acta, 271,* 1-15. https://doi.org/10.1016/j.gca.2019.12.010

Shang, N., Liu, J., Han, Q., Jia, R., & Zhao, S. (2023). Mineralogy and Geochemistry of the Middle Jurassic Coal from the Hexi Mine, Shenfu Mining Area, Ordos Basin: With an Emphasis on Genetic Indications of Siderite. *International Journal of Coal Geology, 279,* Article ID: 104384. https://doi.org/10.1016/j.coal.2023.104384

Stel, H. (2009). Diagenetic Crystallization and Oxidation of Siderite in Red Bed (Buntsandstein) Sediments from the Central Iberian Chain, Spain. *Sedimentary Geology, 213,* 89-96. https://doi.org/10.1016/j.sedgeo.2008.12.001

Tian, H., Li, H., Liu, H., Zhang, J., Zhou, H., Zhang, K., Xiang, Z., Qu, L., & Wang, Z. (2018). Characteristics of C and O Isotopes of the Shennongjia Group in the Northern Margin of the Yangtze Craton and Their Constraints on Paleoenvironment and Depositional Age. *Acta Geologica Sinica, 92,* 2508-2533.

Vuillemin, A., Wirth, R., Kemnitz, H., Schleicher, A. M., Friese, A., Bauer, K. W. et al. (2019). Formation of Diagenetic Siderite in Modern Ferruginous Sediments. *Geology, 47,* 540-544. https://doi.org/10.1130/g46100.1

Wang, S., Shao, L., Wang, D., Sun, Q., Sun, B., & Lu, J. (2019). Sequence Stratigraphy and Coal Accumulation of Lower Cretaceous Coal-Bearing Series in Erlian Basin, Northeastern China. *AAPG Bulletin, 103,* 1653-1690. https://doi.org/10.1306/11211817175

Weibel, R., Lindström, S., Pedersen, G. K., Johansson, L., Dybkjær, K., Whitehouse, M. J. et al. (2016). Groundwater Table Fluctuations Recorded in Zonation of Microbial Siderites from End-Triassic Strata. *Sedimentary Geology, 342,* 47-65. https://doi.org/10.1016/j.sedgeo.2016.06.009

Xi, K., Cao, Y., Lin, M., Liu, K., Wu, S., Yuan, G. et al. (2019). Applications of Light Stable Isotopes (C, O, H) in the Study of Sandstone Diagenesis: A Review. *Acta Geologica Sinica-English Edition, 93,* 213-226. https://doi.org/10.1111/1755-6724.13769

Yang, T., Shen, Y., Qin, Y., Zhang, Y., Lu, L., Jin, J. et al. (2021). Genetic Mechanism and Environment Implications of Siderites in the Lopingian Coal-Bearing Series, Western Guizhou of China: Constrained by Whole-Rock and *in Situ* Geochemistry. *Frontiers in Earth Science, 9,* Article ID: 779991. https://doi.org/10.3389/feart.2021.779991

Zhang, Y., Li, Z., Qin, M., Yang, Z., Liu, R., Li, Z. et al. (2023). Reducing-Condition Reworked Phosphorite Sedimentary Model: Petrographic and Geochemical Evidence from the Lower Cretaceous in the Thaniyat Area, Northern Saudi Arabia. *Sedimentary Geology, 456,* Article ID: 106501. https://doi.org/10.1016/j.sedgeo.2023.106501